



Deposited via The University of Sheffield.

White Rose Research Online URL for this paper:

<https://eprints.whiterose.ac.uk/id/eprint/97243/>

Version: Submitted Version

Article:

Murray, T., Nettles, M., Selmes, N. et al. (2015) Reverse glacier motion during iceberg calving and the cause of glacial earthquakes. *Science*, 349 (6245). pp. 305-308. ISSN: 0036-8075

<https://doi.org/10.1126/science.aab0460>

Reuse

Items deposited in White Rose Research Online are protected by copyright, with all rights reserved unless indicated otherwise. They may be downloaded and/or printed for private study, or other acts as permitted by national copyright laws. The publisher or other rights holders may allow further reproduction and re-use of the full text version. This is indicated by the licence information on the White Rose Research Online record for the item.

Takedown

If you consider content in White Rose Research Online to be in breach of UK law, please notify us by emailing eprints@whiterose.ac.uk including the URL of the record and the reason for the withdrawal request.

1 **Title:**

2
3 **Reverse glacier motion during iceberg calving and the cause of glacial earthquakes**

4
5 **Authors:**

6
7 T. Murray^{1*}, M. Nettles², N. Selmes¹, L. M. Cathles³, J. C. Burton⁴, T. D. James¹, S. Edwards⁵,
8 I. Martin⁵, T. O'Farrell⁶, R. Aspey⁶, I. Rutt¹, and T. Baugé⁷

9
10 **Affiliations:**

11 ¹Glaciology Group, Department of Geography, College of Science, Swansea University,
12 Swansea SA2 8PP, UK

13 ²Lamont-Doherty Earth Observatory, Columbia University, New York, NY 10964 USA

14 ³Department of Atmospheric, Oceanic and Space Sciences, University of Michigan, Ann Arbor,
15 MI 48109 USA

16 ⁴Department of Physics, Emory University, Atlanta, GA 30322 USA

17 ⁵School of Civil Engineering and Geosciences, Newcastle University, Newcastle upon Tyne,
18 NE1 7RU, UK

19 ⁶Department of Electronic and Electrical Engineering, University of Sheffield, Sheffield S1 3JD,
20 UK

21 ⁷Thales, Research & Technology, Worton Drive, Reading, Berkshire, RG2 0SB, UK

22 *Correspondence to: t.murray@swansea.ac.uk

23
24
25
26
27
28
29
30
31
32
33
34

35 **Abstract:**

36 Nearly half of Greenland's mass loss occurs through iceberg calving, but the physical
37 mechanisms operating during calving are poorly known and *in situ* observations are sparse. We
38 show that calving at Greenland's Helheim Glacier causes a minutes-long reversal of the glacier's
39 horizontal flow and a downward deflection of its terminus. The reverse motion results from the
40 horizontal force caused by iceberg capsize and acceleration away from the glacier front. The
41 downward motion results from a hydrodynamic pressure drop behind the capsizing berg, which
42 also causes an upward force on the solid Earth. These forces are the source of glacial
43 earthquakes, globally detectable seismic events whose proper interpretation will allow remote
44 sensing of calving processes occurring at an increasing number of outlet glaciers in Greenland
45 and Antarctica.

46 **Main Text:**

47 One third to one half of Greenland's total mass loss occurs through iceberg calving at the
48 margins of tidewater-terminating glaciers (1, 2). Recent, rapid changes in glacier dynamics are
49 associated with increased calving rates (3-5) and increased rates of glacial earthquakes (6). At
50 large glaciers with near-grounded termini, calving typically occurs when buoyancy forces cause
51 icebergs the full thickness of the glacier to capsize against the calving front (6-9). This type of
52 calving is associated with glacial earthquakes (6, 7, 10), long-period seismic emissions of
53 magnitude ~5 that are observed globally (11). The earthquakes have expanded northward and
54 increased seven-fold in number during the last two decades (6, 12, 13), tracking changes in
55 glacier dynamics, the retreat of glacier fronts, and increased mass loss (6, 14). Buoyancy-driven
56 calving represents an increasingly important source of dynamic mass loss (6-8) as glacier fronts
57 throughout Greenland have retreated to positions near their grounding lines (15). However, due

58 to the difficulty of instrumenting the immediate near-terminus region of these highly active
59 glaciers, few direct observations of the calving process are available, limiting development of the
60 deterministic calving models required for improved understanding of controls on dynamic ice-
61 mass loss. Detailed knowledge of the glacial-earthquake source would allow quantification of
62 calving processes at a large class of Greenland glaciers as well as in several regions of Antarctica
63 (13).

64 Agreement on the source mechanism of glacial earthquakes is limited. Analysis of long-
65 period seismic data shows that a sub-horizontal force acts approximately perpendicular to the
66 glacier calving front during the earthquakes (6, 13). The observed seismic signal is generated
67 over a period of one minute or more (6, 11, 16), much longer than the source duration for
68 tectonic earthquakes of similar size (17). Some authors favor a model in which momentum
69 transfer produces a force acting in the upglacier and then downglacier directions as a newly
70 calved iceberg overturns, accelerates away from the calving front and subsequently decelerates
71 (6, 10, 13). Others suggest that the seismic signal arises from the iceberg scraping along the
72 calving front or fjord bottom (7) or colliding with the glacier terminus (18). Hydrodynamic
73 interactions with fjord water may be important (19) but are little explored. Analytical
74 investigations admit more than one possible mechanism for the earthquakes (20), and no
75 persuasive explanation has been presented for the vertical component of the earthquake force.
76 Here, we combine geodetic, seismic and laboratory data to identify the forces acting during
77 calving at large glaciers and document the source of the associated seismic signals.

78 We recorded geodetic data at the calving margin of Helheim Glacier (Fig. 1) (9), a major
79 outlet of the Greenland Ice Sheet, during 55 days in July-September 2013. A wireless network of
80 on-ice GPS sensors (21) captured glacier motion with cm-level accuracy at positions very close

81 to the calving front at a high temporal sampling rate (22). Hourly images from two cameras
82 located ~4 km down-fjord from and looking at the calving front were used in stereo
83 configuration to obtain the 3D geometry of the calving front and calved icebergs (8, 22). Data
84 from the global seismographic network were analysed for the same time period to identify glacial
85 earthquakes (13, 23) and obtain source parameters (11) including the orientation of the force
86 active during the earthquake, the earthquake centroid-single-force (CSF) amplitude, and the
87 earthquake centroid time, t_c (centroid of the temporal force history) (22).

88 The glacier retreated ~1.5 km in a series of calving events during the observing period.
89 We identified ten large calving events from the camera images. All coincided with glacial
90 earthquakes; in two cases, two earthquakes occurred between subsequent images. During the
91 earthquakes, the region near the calving front shows a dramatic reversal of flow, moving
92 upglacier for several minutes while simultaneously moving downward (Fig. 2, Fig. S1). The
93 horizontal and vertical motion then rebound rapidly.

94 Observations from a glacial earthquake occurring on Day of Year (DOY) 206 at 03:13:47
95 are shown in Figs. 2A and 2C. Analysis of camera images indicates ice loss of $0.461 \pm 0.009 \text{ km}^2$
96 (Fig. 1) at a location of ice thickness 0.79 km, yielding an iceberg volume of 0.36 km^3 with
97 aspect ratio 0.23. The earthquake had CSF amplitude $0.24 \times 10^{14} \text{ kg-m}$, with the force oriented
98 64°W (Fig. 1) and 9° above the horizontal. GPS sensor 1 (Fig. 1) showed a pre-earthquake flow
99 speed of 29 m/day. Immediately prior to the earthquake centroid time, the sensor reversed its
100 direction and moved upglacier at ~40 m/day (displacement 9 cm) and downward (displacement
101 10 cm). The reversed motion was sustained for ~200 seconds and was followed by a downglacier
102 rebound at ~190 m/day (displacement 20 cm) and upward movement (16 cm) for ~90 seconds.
103 Similar temporally coincident signals are seen on nearby sensors 6 and 15 (Fig. 1, Fig. S1).

104 Figures 2B and 2D show glacier deflection for a calving event on DOY 212 (Fig. 1). We
105 observe similar responses for all glacial-earthquake / calving events during which GPS sensors
106 recording data of adequate quality were located within 500 m of the calved block (a total of 9
107 glacial earthquakes and 8 image pairs). These events occurred on DOY 205, 206 (three events),
108 207, 211, 212, and 226 and are observed on multiple GPS sensors (further examples in Fig. S1).

109 The earthquake centroid times occur at or near the end of the glacier's rapid rebound
110 phase, such that the upglacier earthquake force aligns in time with the reverse motion of the
111 glacier. The horizontal glacier deflection is consistent with a model in which the reaction force
112 on the glacier due to seaward acceleration of the newly calved iceberg compresses the glacier
113 front elastically. The front then rebounds as the force decreases and reverses polarity during
114 iceberg deceleration. The glacier front thus acts as a spring, compressing and re-extending in
115 phase with the applied force, which is the horizontal component of the seismic source.

116 The downward deflection of the glacier front occurs in a region where vertical motion of
117 the GPS sensors at tidal frequencies shows the glacier is ungrounded and seawater is present
118 beneath it. Iceberg rotation is likely to cause a low-pressure zone in the opening cavity between
119 the iceberg and the glacier front. This pressure decrease would lower the load on the bedrock,
120 resulting in an upward force acting on the solid Earth, as observed in our seismic analysis. A
121 pressure decrease near the calving front would apply a net downward force on the glacier
122 terminus, lowering the glacier surface in a manner similar to that occurring twice each day when
123 the ocean tides draw down the water level. At sensors experiencing earthquake deflections, we
124 observe variations in vertical position due to the water tide of ~ 0.1 m per 1 m of tidal variation.
125 The calving-related deflection of the glacier surface is ~ 0.1 - 0.16 m, suggesting a change in water
126 pressure equivalent to a water-height change of ~ 1 - 1.6 m, or roughly 1 - 2×10^4 Pa.

127 No observations of pressure or water-level variations are available from the region in the
128 fjord immediately in front of the glacier, where thick ice mélange (Fig. 1) prohibits
129 instrumentation. However, results from analog laboratory experiments allow us to evaluate our
130 inferences (22). A model glacier “terminus” was secured at one end of a water-filled tank, and
131 plastic “icebergs” made from low-density polyethylene were placed flush against the terminus
132 and allowed to capsize spontaneously under the influence of gravitational and buoyancy forces
133 (24; Fig. 3). Sensors embedded in the model glacier terminus monitored pressure in the water
134 column and the force exerted on the terminus during iceberg capsize.

135 The measured force on the terminus as the iceberg begins to capsize is oriented in the
136 upglacier direction and slowly increases as the iceberg rotates. As the iceberg nears horizontal,
137 the force decreases rapidly. Pressure at the terminus decreases as the iceberg rotates, increasing
138 again as the iceberg nears horizontal. Once the iceberg loses contact with the terminus, the
139 measured force and pressure begin to oscillate due to induced wave action in the tank.

140 We scaled up the measured forces and pressures to match the dimensions of icebergs
141 calved at Helheim Glacier (Fig. 3). The laboratory data scale by powers of the ratio of the
142 iceberg height in the field to the iceberg height in the laboratory (19,24). The scaled peak force
143 agrees well with typical values inferred from earthquake analysis ($\sim 10^{11}$ N). The scaled peak
144 pressure drop ($\sim 5 \times 10^4$ Pa) applied over an area corresponding to the iceberg’s map-view
145 dimensions yields an upward-directed force consistent with the seismically inferred vertical force
146 component, such that the total force acting on the solid Earth is oriented $\sim 10^\circ$ above the
147 horizontal. Computation and inversion of synthetic seismograms from the scaled force and
148 pressure data confirms the consistency of the laboratory model with real-world data.

149 We use the scaled force and pressure to predict the deformation of the terminus region
150 (22). The total force F_{tot} per unit area A_F acting on the calving region produces a horizontal,
151 linear deflection orthogonal to the calving front $F_{\text{tot}}/A_F = E\Delta L/L$, where E is the Young's
152 modulus of glacial ice. The value of L is chosen to provide the best match to the glacier position
153 data. This length-scale likely represents the distance from the terminus to the grounding zone.
154 We model the ungrounded section of the glacier as an elastic beam of length L loaded by the
155 vertical force due to the pressure drop. The inferred distances L are a few km, consistent with
156 values estimated from GPS data.

157 Glacier displacements predicted from the scaled laboratory data for iceberg dimensions
158 corresponding to a calving event on DOY 206 (Fig. 1, Fig. 2A) are shown in Fig. 3. Agreement
159 with the observed glacier displacement is very good, particularly during the time over which the
160 force acts in the upglacier direction (until the earthquake centroid time). After this time, the
161 laboratory-derived prediction is dominated by oscillations of the water column in the tank, which
162 does not contain the thick layer of ice mélange present in Helheim Fjord and expected to damp
163 such high-frequency oscillations.

164 We conclude that as large icebergs rotate and accelerate away from the glacier calving
165 front (Fig. 4), the reaction force, which is the horizontal component of the earthquake force,
166 compresses the glacier front elastically, overcoming normal downglacier flow and temporarily
167 reversing the motion of the glacier. Hydrodynamic interaction of the iceberg with the fjord water
168 rapidly reduces pressure behind the rotating iceberg, resulting in an upward force on the solid
169 Earth that is the vertical force observed in the earthquake. The lowered water pressure draws
170 down the ungrounded glacier margin, pulling the glacier surface downward during the
171 earthquake.

172 Our results document the forces active during an increasingly important class of calving
173 events and definitively identify the processes that cause glacial earthquakes. This understanding
174 of glacier calving and glacial earthquakes opens the potential for remote, quantitative
175 characterisation of iceberg calving and calving rates, as well as improved models for ice-ocean
176 interaction.

177 **References and Notes:**

- 178 1. M. van den Broeke *et al.*, Partitioning recent Greenland mass loss. *Science* **326**, 984-986
179 (2009).
- 180 2. E. M. Enderlin *et al.*, An improved mass budget for the Greenland ice sheet. *Geophys. Res.*
181 *Lett.* **41**, 866-872 (2014).
- 182 3. I. Joughin, W. Abdalati, M. Fahnestock, Large fluctuations in speed on Greenland's
183 Jakobshavn Isbræ glacier. *Nature* **432**, 608-610 (2004).
- 184 4. A. Luckman, T. Murray, R. de Lange, E. Hanna, Rapid and synchronous ice-dynamic
185 changes in East Greenland. *Geophys. Res. Lett.* **33**, L03503 (2006).
- 186 5. I. M. Howat, I. Joughin, T. A. Scambos, Rapid changes in ice discharge from Greenland
187 outlet glaciers. *Science* **315**, 1559-1561 (2007).
- 188 6. S. A. Veitch, M. Nettles, Spatial and temporal variations in Greenland glacial-earthquake
189 activity, 1993-2010. *J. Geophys. Res.* **117**, F04007 (2012).
- 190 7. J. M. Amundson *et al.*, Glacier, fjord, and seismic response to recent large calving events,
191 Jakobshavn Isbrae, Greenland. *Geophys. Res. Lett.* **35**, L22501 (2008).
- 192 8. T. D. James, T. Murray, N. Selmes, K. Scharrer, M. E. O'Leary, Buoyant flexure and basal
193 crevassing in dynamic mass loss at Helheim Glacier. *Nature Geosci.* **7**, 593-596 (2014).
- 194 9. M. Nettles *et al.*, Step-wise changes in glacier flow speed coincide with calving and glacial
195 earthquakes at Helheim Glacier, Greenland. *Geophys. Res. Lett.* **35**, L24503 (2008).
- 196 10. G. Ekström, M. Nettles, G. A. Abers, Glacial earthquakes. *Science* **302**, 622-624 (2003).
- 197 11. G. Ekström, M. Nettles, V. C. Tsai, Seasonality and increasing frequency of Greenland
198 glacial earthquakes. *Science* **311**, 1756-1758 (2006).
- 199 12. M. Nettles, G. Ekström, Glacial earthquakes in Greenland and Antarctica. *Ann. Rev. Earth*
200 *Planet. Sci.* **38**, 467-491 (2010).
- 201 13. I. Joughin *et al.*, Ice-front variation and tidewater behavior on Helheim and Kangerdlugssuaq
202 Glaciers, Greenland. *J. Geophys. Res.*, **113**, F01004 (2008).
- 203 14. I. M. Howat, A. Eddy, Multi-decadal retreat of Greenland's marine-terminating glaciers. *J.*
204 *Glaciol.*, **57**, 389-396 (2011).
- 205 15. V. C. Tsai, G. Ekström, Analysis of glacial earthquakes. *J. Geophys. Res.* **112**, F03S22
206 (2007).

- 207 16. G. Ekström, E. R. Engdahl, Earthquake source parameters and stress distribution in the Adak
208 Island region of the central Aleutian Islands, Alaska. *J. Geophys. Res.* **94**, 15,499-15,519
209 (1989).
- 210 17. F. Walter *et al.*, Analysis of low-frequency seismic signals generated during a multiple-
211 iceberg calving event at Jakobshavn Isbræ, Greenland. *J. Geophys. Res.* **117**, F01036 (2012).
- 212 18. J. M. Amundson, J. C. Burton, S. Correa-Legisos, Impact of hydrodynamics on seismic
213 signals generated by iceberg collisions. *Ann. Glaciol.* **53**, 106–112 (2012).
- 214 19. V. C. Tsai, J. R. Rice, M. Fahnestock, Possible mechanisms for glacial earthquakes. *J.*
215 *Geophys. Res.* **113**, F03014 (2008).
- 216 20. I. Martin *et al.*, High-resolution sensor network for monitoring glacier dynamics. *IEEE*
217 *Sensors J.* **14**, 3926-3931 (2014).
- 218 21. Materials and methods are available as supplementary materials on *Science Online*.
- 219 22. G. Ekström, Global detection and location of seismic sources by using surface waves. *Bull.*
220 *Seism. Soc. Am.* **96**, 1201-1212 (2006).
- 221 23. J. C. Burton *et al.*, Laboratory investigations of iceberg capsizing dynamics, energy dissipation
222 and tsunamigenesis. *J. Geophys. Res.* **117**, F01007 (2012).
- 223 24. H. Kawakatsu, Centroid single force inversion of seismic waves generated by landslides. *J.*
224 *Geophys. Res.* **94**, 12363-12374 (1989).
- 225 25. A. M. Dziewonski, D. L. Anderson, Preliminary reference Earth model. *Phys. Earth Planet.*
226 *Inter.* **25**, 297-356 (1981).
- 227 26. T. D. James, T. Murray, N. E. Barrand, S. L. Barr, Extracting photogrammetric ground
228 control from lidar DEMs for change detection. *Photogramm. Rec.* **21**, 310-326 (2006).
- 229 27. C. Leuschen, C. Allen, IceBridge MCoRDS L3 Gridded Ice Thickness, Surface, and Bottom,
230 Version 2, Helheim_2008_2012_Composite. Boulder, Colorado USA: NASA DAAC at the
231 National Snow and Ice Data Center. <http://nsidc.org/data/irmcr3.html> (2013).
- 232 28. J. F. Zumberge, M. B. Hefflin, D. C. Jefferson, M. M. Watkins, F. H. Webb, Precise point
233 positioning for the efficient and robust analysis of GPS data from large networks. *J.*
234 *Geophys. Res.* **102**, 5005-5017 (1997).
- 235 29. J. Saastamoinen, Contributions to the theory of atmospheric refraction. *Bull. Geodesique* **107**,
236 13-34 (1973).
- 237 30. J. Boehm, A. Niell, P. Tregoning, H. Schuh, Global Mapping Function (GMF): A new
238 empirical mapping function based on numerical weather model data. *Geophys. Res. Lett.* **33**,
239 L07304 (2006).
- 240 31. F. Lyard, F. Lefevre, T. Letellier, O. Francis, Modelling the global ocean tides: modern
241 insights from FES2004. *Ocean Dynamics* **56**, 394-415 (2006).
- 242 32. IERS Conventions (2010). G. Petit and B. Luzum (eds.). (IERS Technical Note ; 36)
243 Frankfurt am Main: Verlag des Bundesamts für Kartographie und Geodäsie,. 179 pp. (2010).
- 244 33. W. Bertiger *et al.*, Single receiver phase ambiguity resolution with GPS data. *J. Geod.* **84**,
245 327-337 (2010).

- 246 34. G. Chen, GPS kinematic positioning for the airborne laser altimetry at Long Valley,
247 California. Ph.D. thesis, Mass. Inst. of Technol., Cambridge (1998).
- 248 35. R. Dach *et al.*, GNSS processing at CODE: status report. *J. Geod.* **83**, 353-365 (2009).
- 249 36. J. C. Burton, L. M. Cathles, W. G. Wilder, The role of cooperative iceberg capsizes in ice-
250 shelf disintegration. *Annals Glaciol.* **54**, 84-90 (2013).
- 251 37. I. H. Cho, M. H. Kim, Wave absorbing system using inclined perforated plates. *J. Fluid*
252 *Mech.* **606**, 1-20 (2008).
- 253 38. D. R. MacAyeal, D. S. Abbot, O. V. Sergienko, Iceberg-capsizes tsunamigenesis. *Annals*
254 *Glaciol.* **52**, 51-56 (2011).
- 255 39. D. G. Vaughan, Tidal flexure at ice shelf margins. *J. Geophys. Res.* **100**, 6213-6224 (1995).
- 256 40. E. Rignot, Tidal motion, ice velocity and melt rate at Petermann Gletscher, Greenland,
257 measured from radar interferometry. *J. Glaciol.* **42**, 476-485 (1996).

258 **Acknowledgments:**

259 This work was supported by the Natural Environment Research Council UK grant
260 NE/I007148/1. TM is currently supported by a Royal Society Leverhulme Trust Senior Research
261 Fellowship. TDJ was supported by the Climate Change Consortium of Wales (C3W). MN was
262 supported by US National Science Foundation (NSF) grant EAR 12-49167. LMC is currently
263 supported by the Michigan Society of Fellows. JB and LMC were supported and the laboratory
264 equipment was developed with support from NSF grant ANT 0944193. A. Everett is thanked for
265 assistance in the field and L. Kaluziński for assistance with laboratory data. We acknowledge
266 the use of bed data from CReSIS generated with support from NSF grant ANT-0424589 and
267 NASA grant NNX10AT68G, and the use of seismic data from the IRIS-USGS Global
268 Seismographic Network, Geoscope, Geofon, Mednet, and GLISN. A 2013 lidar survey flown by
269 the NERC Airborne Remote Sensing Facility was used in the processing of photographs. Seismic
270 waveforms are available from the IRIS Data Management Center; GPS data are available from
271 the authors.
272

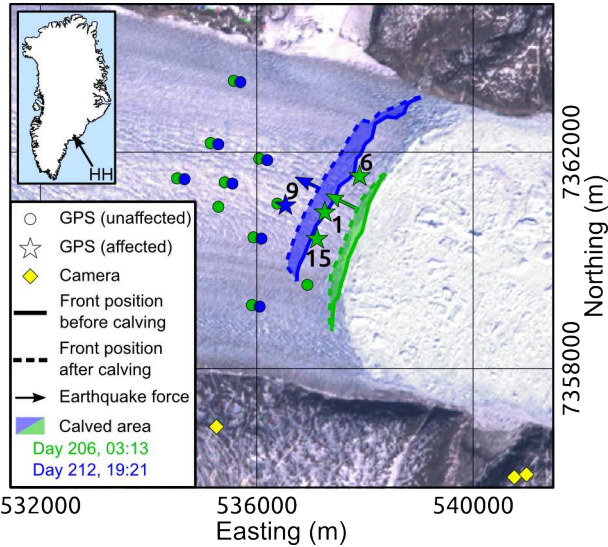
273 **Supplementary Materials:**

274 Materials and Methods

275 Figure S1

276 References (25-41)

277



278

279

280

281

282

283

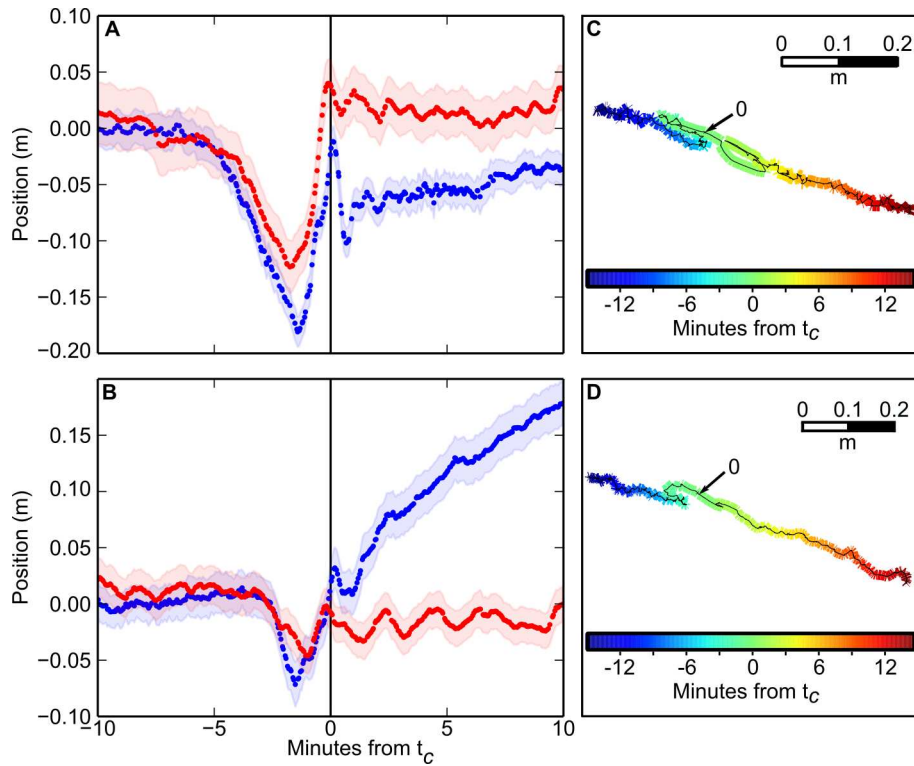
284

285

286

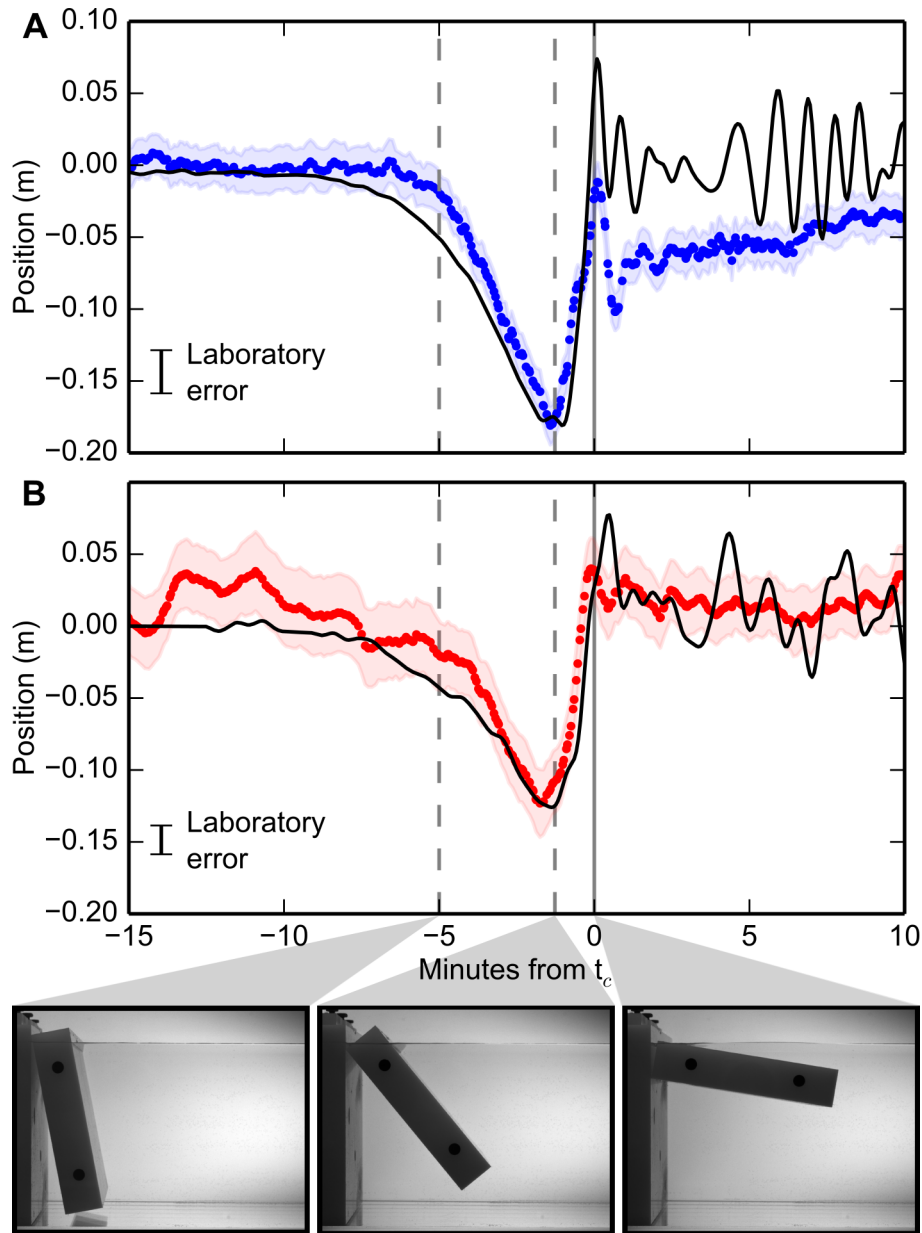
287

Fig. 1. Helheim Glacier, position of sensors, and seismic force directions. Location of GPS sensors and icebergs calved at Helheim Glacier (HH) for glacial-earthquake events at 03:13 DOY 206 2013 and 19:21 DOY 212 2013, superimposed on Landsat 7 image from DOY 167 2013. ‘Affected’ sensors exhibit earthquake-related deflections. Scan-line-corrector failure stripes have been removed for clarity. Glacier flow from left to right; bright white mélange (mix of iceberg fragments and sea ice) can be seen in front of calving margin. Calving-front positions obtained from photogrammetric DEMs derived from cameras. Times are UTC, positions are meters UTM zone 24N.



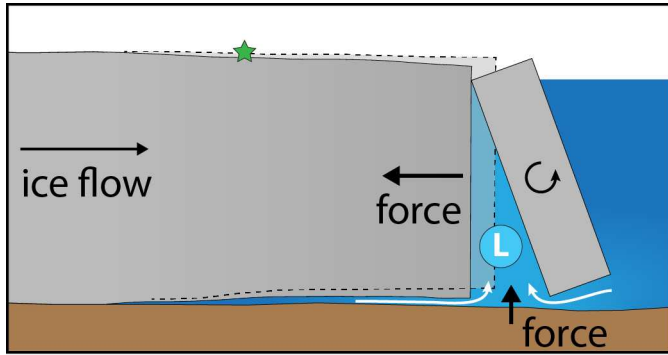
288

289 **Fig. 2. Response of GPS sensors on glacier at the time of glacial earthquakes.** (A) Sensor 1 at
 290 03:13 on DOY 206 2013. (B) Sensor 9 at 19:21 on DOY 212 2013. Blue dots show detrended
 291 along-flow displacement, red dots show height. Shading shows 1σ position errors. Earthquake
 292 centroid time t_c . Horizontal displacement has trend from 30-10 mins before t_c removed (A=28.9
 293 m/day, B=24.6 m/day). Height has mean removed. (C) and (D) Plan view of GPS traces shown
 294 in (A) and (B) during 30 minutes around t_c , marked as 0.
 295



296

297 **Fig. 3. Scaled laboratory data from glacier “terminus” during “iceberg” capsize event**
 298 **compared to field observations. (A) Horizontal displacement scaled from force (black line)**
 299 **compared to downflow GPS data (blue). (B) Vertical displacement scaled from pressure (black line)**
 300 **compared to vertical GPS data (red). Errors in laboratory data are standard deviation from**
 301 **repeated capsize events. GPS data as in Figure 2A. Photographs show stage of capsize at times**
 302 **marked by dashed lines and (solid gray line) t_c . Aspect ratio of model iceberg is 0.22.**
 303



304

305 **Fig. 4. Cartoon of glacier terminus during calving event.** Glacier deflection caused by
 306 capsizing iceberg shown relative to initial position (dotted line). Acceleration of iceberg to right
 307 exerts a force in the upglacier direction (left), leading to reverse motion of the GPS sensors
 308 (green star). Reduced pressure behind the iceberg (“L”) draws water from beneath the glacier
 309 and from the proglacial fjord, pulling the floating portion of the glacier downward and exerting
 310 an upward force on the solid Earth.